MANUSCRIPT FOR SUBMISSION TO: *MOLECULAR IMAGING AND BIOLOGY*

Molecular imaging of a Zirconium-89-labeled antibody targeting *Plasmodium falciparum*-infected human erythrocytes

Janie Duvenhage[1,3], Thomas Ebenhan[2,3], Seike Garny[1], Ignacio Hernández González[4], René Leyva Montaña[5], Roger Prise[8], Lyn-Marie Birkholtz[1], Jan Rijn Zeevaart[3,7] *

[1]*Department of Biochemistry, Genetics and Microbiology, Institute of Sustainable Malaria Control, University of Pretoria, Pretoria, South Africa*

[2]*Department of Nuclear Medicine, University of Pretoria, Pretoria, South Africa*

[3]*Preclinical Imaging Facility, The South African Nuclear Energy Corporation SOC Ltd (Necsa), Pelindaba, South Africa*

[4]*Department of Development and* [5]*Deparment of Radiopharmacy, Center of Isotopes, Havana, Cuba*

[6]*Rapid Laboratories, Sir Charles Gairdner Hospital, Perth, Western Australia*

[7]*Preclinical Drug Development Platform, North West University, Potchefstroom, South Africa*

[8]*Department of Physics, University of Western Australia, Australia*

Correspondence:

** Jan Rijn Zeevaart*

janrijn.zeevaart@necsa.co.za

+27 12 305 5786

Running title: Radiolabeling malaria antibodies

Manuscript category: Article

Abstract

Purpose: Nuclear imaging is an important pre-clinical research tool to study infectious diseases *in vivo,* and could be extended to investigate complex aspects of malaria infections. As such, we report for the first time successful radiolabeling of a novel antibody specific to *Plasmodium*-infected erythrocytes (IIIB6), it's *in vitro* assessment and molecular imaging in nude mice.

Procedures: *In vitro* confocal microscopy was used to determine the stage-specificity of *Plasmodium*- infected erythrocytes recognised by IIIB6. To enable micro-PET/CT imaging, IIIB6 was conjugated to Bz-DFO-NCS and subsequently radiolabeled with zirconium-89. Healthy nude mice were injected with [^{89}Zr]IIIB6 and pharmacokinetics and organ uptake were monitored over 24 hours. This was followed by post mortem animal dissection to determine the biodistribution of [^{89}Zr]IIIB6.

Results: IIIB6 recognised all the relevant stages of *Plasmodium falciparum*-infected erythrocytes (trophozoites, schizonts and gametocytes) that are responsible for severe malaria pathology. [^{89}Zr]IIIB6-radiolabeling yields were efficient at 84%-89%. Blood pool imaging analysis indicated a pharmacological half-life of 9.6 ± 2.5 h for [^{89}Zr]IIIB6. The highest standard uptake values were determined at 2-6 h in the liver followed by the spleen, kidneys, heart, stomach, lung, respectively. Minimal activity was present in muscle- and bone tissue.

Conclusion: *In vitro* characterisation of IIIB6 and pharmacokinetic characterization of [^{89}Zr]IIIB6 revealed that this antibody has potential for future use in *Plasmodium*- infected mouse models to study malaria in a preclinical *in vivo* setting with PET/CT imaging.

Keywords

Plasmodium falciparum, micro-PET/CT imaging, [^{89}Zr]IIIB6, nimotuzumab, zirconium-89

Introduction

Malaria is classified as a poverty-related disease, stretching well beyond the discernible morbidity and public health threat and severely affecting the socio-economic status of a population. Malaria is a blood-borne disease transmitted by *Plasmodium* parasites and the most devastating forms of the disease that accounts for the majority cases and deaths is caused by *Plasmodium falciparum*. Understanding the interplay between the life cycle of the parasite and biological systems within the host is of critical importance for achieving global malaria eradication. Once the mosquito feeds on the human host, it injects *P. falciparum* sporozoites into the bloodstream. The sporozoites migrate to the liver and mature in the hepatocytes to schizonts containing multiple merozoites. After the merozoites are released into the blood stream, these asexual parasites enter the intra-erythrocytic development cycle (IDC). During the IDC, the parasite develops through ring-, throphozoite- and schizont stages by biochemical and metabolic maturation. Schizogony results in endo-mitotic division and production of up to 30 daughter merozoites that are released when the host erythrocyte ruptures. These merozoites can then re-invade erythrocytes and undergo the same developmental stages as described above, multiplying to thousands of parasites in a very short time span. A small proportion of these (<30%) develop into male and female gametocytes, which can again be ingested by a vector mosquito when it feeds on a human host to complete the cycle [1]. The IDC in the human host is responsible for the development, blood stage survival and virulence-associated pathogenicity of the disease [2, 3]. One major obstacle in understanding these aspects of parasite biology is the inability to visualise and observe the intricate host-parasite mechanisms that govern malaria pathogenicity *in vivo* in real time, with most studies limited to optical imaging (bioluminescence and fluorescence) of *P. berghei* and *P. yoelii* infection in mouse models. The latter involves genetically

manipulated rodent parasites [4] which do not accurately represent human malaria parasite pathology.

Magnetic resonance imaging (MRI) and computed tomography (CT) have been used to study cerebral malaria in humans but these anatomical imaging modalities lack sensitivity and specificity to severe malaria [5].

Comparatively, nuclear imaging offers great sensitivity and selectivity, allows the early detection and diagnosis of a disease and tracking disease progression or efficacy of therapeutic interventions. Positron emission tomography (PET) imaging using 2-deoxy-[^{18} F]fluoro-D-glucose ([^{18}F]FDG) is used routinely in oncological pathology, central nervous system disorders, cardiovascular disease and infectious diseases [6]. The clinical evaluation of *Mycobacterium tuberculosis* (TB) and human immune deficiency virus (HIV) infections revealed [^{18}F]FDG-PET/CT as a useful non-invasive method to image disease onset, progression and response to the drug treatment in real time [7, 8]. [^{18}F]FDG-PET/CT has been applied in malaria where *Plasmodium coatnyei*-infected Japanese macaques showed high splenic glucose uptake and a reduced glucose metabolism in the cerebral cortex during acute infection [9, 10]. However, [^{18}F]FDG-PET/CT is not disease specific and this can lead to false positives or negatives in image interpretation, particularly when co-infection or underlying diseases pathology exists. Nuclear imaging does not only allow to study the presence of a disease, but also to study pathophysiological events and metabolic processes of the disease e.g. deposition of amyloid-beta plaques in Alzheimer's disease [11].

Target-specific nuclear imaging includes the use of monoclonal antibodies to provide very stable and target-specific PET imaging agents, making them epitope-specific carriers of radionuclides to the site of interest [12]. For instance, CIMAher® (Nimotuzumab, h-R3) is a well studied stable monoclonal antibody approved for human use in tumor imaging and cancer by targeting EGFR (epidermal growth factor receptor) binding [13]. Once

radiolabeled, the antibody affords the opportunity to be a selective diagnostic radiotracer and is particularly useful in ovarian cancer diagnosis due to the overexpression of EGFR. The advantages of such target-specific imaging strategies have not been explored to specifically trace malaria infections in humans.

This investigation therefore aimed to determine if IIIB6, a novel antibody specific to *P. falciparum*-infected erythrocytes, could be a viable molecular imaging tracer for the parasite in malaria infections. We herein demonstrate the zirconium-89 (Zr-89) conjugation and radiolabeling of IIIB6 *in vitro*, and *in vivo* characterisation (pharmacokinetics, biodistribution and stability) of the Zr-89 labeled IIIB6 antibody ([^{89}Zr]IIIB6). Developing tools such as radiolabeled antibodies to be used for PET-imaging, are essential to further the development of novel antimalarials, diagnostics and identification of epidemiological biomarkers [14].

Materials and methods

All materials and reagents used in *in vitro* experiments were obtained from Sigma Aldrich unless otherwise stated. IIIB6 (and IIIB6-Alexa Fluor 647), a ~1000 kDa mouse IgM-isotype monoclonal antibody targeting all stages of *P. falciparum*-infected erythrocytes, was purchased from Novus Biologicals (Littleton, USA). Nimotuzumab (h-R3), a 150 kDa humanized monoclonal antibody (IgG) was purchased from CIMAB S.A. (Havana, Cuba). Zr-89 (half-life 78.4 h) was produced by bombarding Yttrium-89 on a Yttrium foil with 18 MeV protons (p,n) using a 18 MeV cyclotron. Purified [^{89}Zr]oxalate in 0.1 M oxalic acid ($\geq$ 0.156 GBq/nmol) was kindly provided by RAPID Laboratory (Perth, Australia). The chelating agent N1-hydroxy-N1-(5-(4-(hydroxy(5-(3-(4-isothiocyanatophenyl)thioureido) pentyl)amino)-4-oxobutanamido)pentyl)-N4-(5-(N-hydroxyacetamido)pentyl)succinamide (p-NCS-Bz-DFO) was purchased from CheMatech (Dijon, France). Athymic nude mice were obtained from the Charles River Laboratory (Massachusetts, United States).

In vitro characterisation of IIIB6

Cultivation of parasites

Ethical approval for this study was granted by the University of Pretoria Ethical committee (No: 120821-077). *P. falciparum* (strains NF54) were cultivated as previously described at 37°C in human erythrocytes (Type O+ or A+) at a 5% haematocrit [15]. *P. falciparum* cultures (5% haematocrit, >2% parasitaemia) were synchronised using a 5% (w/v) D-sorbitol as described to obtain a >95% ring stage population [16, 17]. Gametocyte cultures were induced from ring stage *P. falciparum* cultures (6–10% parasitaemia, 5% haematocrit) and maintained as previously described [15].

Confocal microscopy parasite imaging of IIIB6

P. falciparum asexual and sexual stage parasites (1% haematocrit, 2% parasitaemia) were visualized using Alexa Fluor 647- labeled IIIB6 antibodies. Samples were fixed onto poly-L-Lysine (0.1 mg/ml) pre-coated coverslips with 0.25% formaldehyde and nonspecific antibody binding sites blocked with PBS-Tween containing 1% (w/v) BSA. The fixed cells were incubated with 1:10 to 1:100 dilutions of IIIB6:Alexa Fluor 647, in PBS-Tween overnight at 4°C in the dark and washed three times with PBS to remove any unbound antibody. Parasites were additionally stained with Hoechst (1:100 dilution) for nuclear detection at room temperature for 30 min, followed by three washes with PBS. The slides were subsequently evaluated using fluorescent confocal microscopy in Fluoroshield with a 510 META confocal laser scanning microscope (Carl Zeiss, Jena, Germany); Alexa Fluor 647 was detected at 665 nm through the META detector and Hoechst detected at 460 – 490 nm with a 420LP filter. Images were analysed with Image J (National Institutes of Health, Bethesda, USA); white field was used to identify infected erythrocytes containing haemozoin crystals.

Preparation and Zr-89 radiolabeling of IIIB6

IIIB6 (MW ~ 1000 kDa, 1 mg/ml in 0.09% sodium azide) was concentrated to 2.5 mg/ml using centrifugal filtration. The Amicon Ultra-0.5 Centrifugal Filter Unit (Merck Millipore, Germany) was prepared by rinsing it with 0.5 ml PBS (0.1 M) with centrifugation (Serie Digicen 21 R, Orto Alresa) for 10 min at 2500*g*. Direct conjugation of NCS-Bz-DFO was achieved by ε-amino group conjugation, utilising the unblocked lysine residue on IIIB6 [18]. NCS-Bz-DFO (6.7 mg/ml in DMSO, pH 8.5) was varied with constant mass of IIIB6 i.e. antibody:NCS-Bz-DFO molar ratios of 1:20 and 1:50 were used. The mixtures were incubated at 37°C for 1 h, whilst shaking gently. The antibody-chelate was purified and concentrated to 1.75 mg/ml using an Amicon Ultra-0.5 filter to. Zr-89 radiolabeling of the antibody was achieved by adopting a previously published procedure [18]. Briefly, 0.1 M ammonium acetate was added to Zr-89 (96 MBq) to adjust the pH to 7. The NCS-Bz-DFO-IIIB6 was added to the Zr-89 solution and incubated for 1 h at 25°C, whilst shaking gently (pH range was kept between 6.8 and 7.2). Instant thin-layer chromatography (iTLC) was performed to determine the radiochemical purity of [^{89}Zr]NCS-Bz-DFO-IIIB6 (denoted as [^{89}Zr]IIIB6) using silica-gel plated strips exposed to a mobile phase consisting of 10% (w/v) ammonium acetate:methanol (1:1).

Preparation and Zr-89 radiolabeling of h-R3

H-R3 (5 mg/ml) was concentrated to 8.9 mg/ml using centrifugal filtration as described for the IIIB6 concentrating procedure. NCS-Bz-DFO (3.3 mg/ml in DMSO, pH 8.5) conjugation to h-R3 was achieved with an antibody:NCS-Bz-DFO molar ratio of 1:2. The mixtures were incubated at 37°C for 1 h, whilst shaking gently. The antibody-chelate was purified and concentrated to 12.45 mg/ml. Zr-89 radiolabeling of h-R3 was achieved as described above with minor adjustments [18]. Ammonium acetate was added to 300 µl Zr-89 (471 MBq) to

adjust the pH to 7. The radiochemical purity of [^{89}Zr]DFO-Bz-SCN-h-R3 (denoted as [^{89}Zr]hR3) was determined by iTLC using silica-gel plated strips exposed to a mobile phase consisting of 10% (w/v) ammonium acetate:methanol (1:1).

In vivo characterization of [^{89}Zr]IIIB6 and [^{89}Zr]h-R3

Animal preparation

Athymic nude BALB/c mice (female, 8-10 weeks-old, 30-48 g) were used for the *in vivo* characterisation of [^{89}Zr]IIIB6. For the *in vivo* characterisation of [^{89}Zr]h-R3, athymic nude BALB/c mice (female, 15-20 g) were used. Animals were anaesthetised for the tracer injection using 2-3% Isoflurane (Isofor(r) Sanofi-Aventis) in oxygen. Similar activities were injected for [^{89}Zr]IIIB6 (7.5 – 15.1 MBq), as for [^{89}Zr]h-R3 (10.9 – 15.1 MBq) and [^{89}Zr]oxalate (8.3 – 11.7 MBq). Injection formulation consisted of saline containing the radiolabeled product. A volume of 0.05-0.15 ml tracer was administered intravenously via the tail vein. For micro-PET/CT imaging of [^{89}Zr]IIIB6, general anaesthesia was administered using 5% isoflurane in oxygen followed by maintaining the animals under anaesthesia with 2-3% isoflurane. Following imaging, the mice were euthanized by blood perfusion while still under anaesthesia.

Micro-PET /CT image acquisition, reconstruction and quantification of [^{89}Zr]IIIB6

Nuclear imaging was performed utilizing a small animal imaging camera (NanoScan PET/CT, Mediso Medical Systems, Hungary) at NECSA, South Africa. Anaesthetised animals were immobilized on the scanner bed (orientation: prone, nose first) for the duration of the scans and body temperature oxygen level and breathing rate were monitored. Following a topogram (35 KVp, 170 ms, max FOK), CT X-ray images were acquired using the following parameters: 50 KVp, 300 ms, max FOK, 360 projections in semi-circular mode, 1:4 binning (medium voxel size and slice thickness; cosine filter) and a matrix size of 250 x 250 x 250. The images served as anatomical reference and allowed for scatter and attenuation

correction during PET data reconstruction. Image guided biodistribution of [^{89}Zr]IIIB6 was determined at 2 h, 4 h, 6 h, and 24 h after tracer injection (20 min image acquisition, 1 bed position). PET image reconstruction was performed from list-mode: reconstruction algorithm 3D OSEM (6 iterations; Terra-Toma 3D), energy window 400–600 keV, coincidence mode 1:5, corrections for random events, detector normalization, decay and dead time and voxel size 0.65 mm. Inter View Fusion software version 2.02.055.2010 (Mediso, Hungary) was used for data visualization, yielding co-registered PET/CT images in axial, coronal and sagittal orientation. Three-dimensional volumes of interest (VOI) were used to determine the percentage of injected dose per gram (%ID/g) and standard uptake value (SUV) (g/ml) in selected organs. Semi-quantified tissue/organ tracer concentrations were used to generate time-activity curves. Area-under-the-curve analysis was used to determine normalised SUV, defined as the regional tissue radioactivity concentration normalised to account for injected dose and body weight of the subject.

Post mortem tracer biodistribution of [^{89}Zr]IIIB6 and [^{89}Zr]h-R3

Following the final image acquisition of [^{89}Zr]IIIB6 and 24 h post injection of [^{89}Zr]h-R3, or [^{89}Zr]oxalate animals were euthanized, organs were dissected, and weighed. The organ- or tissue related activities were determined using an automated gamma counter (Hidex Gamma Counter AMG, Turku, Finland). Alternately, the activity of [^{89}Zr]h-R3 in organs or tissues was determined using a Wizard 2470 automatic gamma counter (Perkin Elmer, USA). Following standard activity corrections for background and radioactive decay, results were expressed as a percentage of the injected dose per gram of tissue or organ (%ID/g).

Biostatistics

If not stated otherwise, results are presented as mean and standard error of mean (SEM) of at least three independent biological replicates. At least 1000 *P. falciparum*-infected erythrocytes were analysed to quantify imaging results. Representative qualitative images are

presented; however all available images was used for quantification. Significance of the biodistribution of [^{89}Zr]IIIB6 and [^{89}Zr]h-R3 and image-derived organ pharmacokinetics of [^{89}Zr]IIIB6 *in vivo* was determined using paired and unpaired student's t tests.

Results

IIIB6 successfully identifies P. falciparum-infected erythrocytes

Confocal imaging indicated successful binding of Alexa Fluor:IIIB6 to *P. falciparum*-infected erythrocytes with little background to uninfected erythrocytes observed. Moreover, the antibody displays reactivity against all the mature stages of both asexual parasites (trophozoites, schizonts) and mature gametocytes (**Figure 1**), but was unable to detect immature ring-stage parasites, likely due to the parasite-derived antigen that was not yet produced in these stages (results not shown).

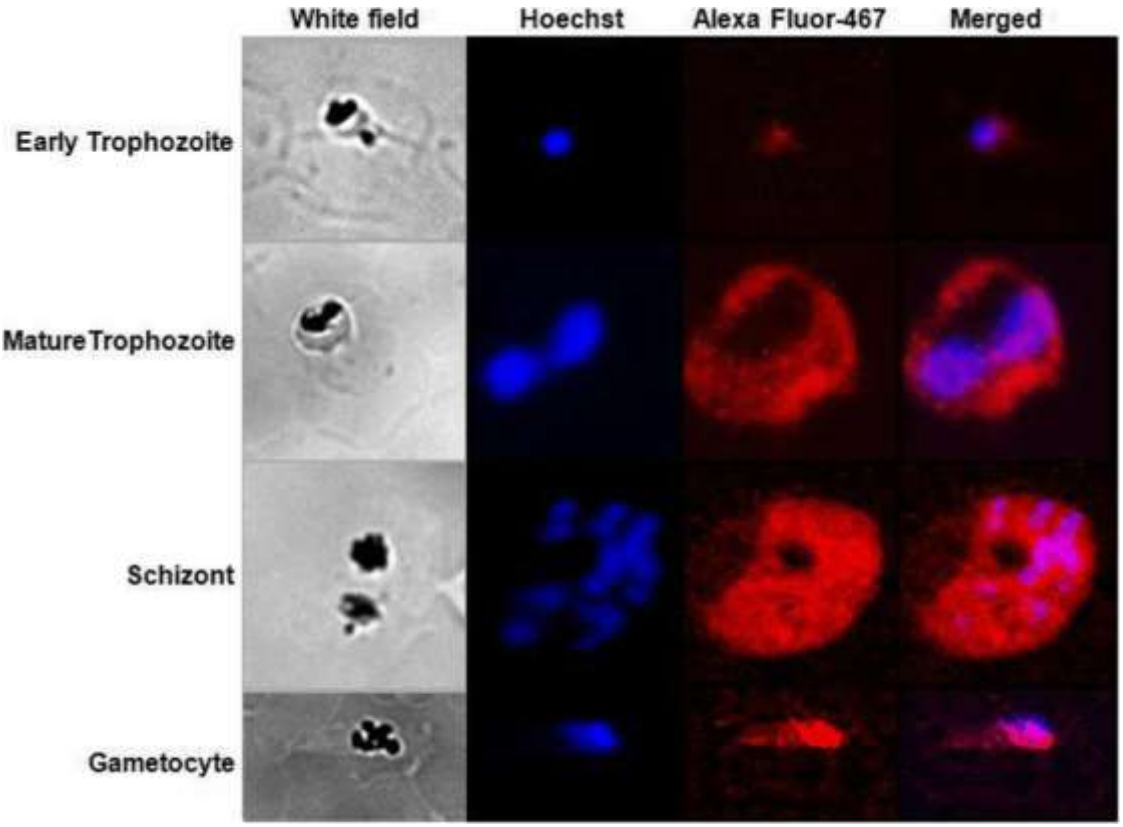

Fig. 1. Confocal microscopic evaluation of IIIB6 binding to different intra-erythrocytic stages of *P. falciparum* parasites. Nuclei were stained with Hoechst and visualised in the blue channel. The IIIB6-Alexa Fluor-647-specific cellular distribution was visualised in the red channel. ImageJ was used for image analyses (National Institutes of Health, Bethesda, USA).

Preparation and Zr-89 radiolabeling of IIIB6 and h-R3

Concentration of IIIB6 by ultracentrifugation improved the efficiency of Zr-89 radiolabeling. Using iTLC, the radiolabeling purity for [^{89}Zr]IIIB6-NCS-Bz-DFO (1:20 ratio of antibody to NCS-Bz-DFO during the conjugation step) improved to 89%, while 11% of the Zr-89 remained in oxalic form and was not bound to the antibody. Antibody:NCS-Bz-DFO ratios higher than 1:20 (e.g. 1:50) did not result in any improvement of labeling efficiency possibly due to saturation. Higher conjugation ratios are not alos desirable due to potential lack of binding selectivity. After centrifugal separation of unbound [^{89}Zr]oxalate, a final desired radiochemical purity of [^{89}Zr]IIIB6 of >98% was achieved with a radiochemical yield at [^{89}Zr]IIIB6 of 40 - 48 MBq and a high tracer concentration of 280 - 320 MBq/ml. More than 95% of [^{89}Zr]IIIB6 was preserved at room temperature and physiological pH for 48 h. This was deemed sufficient to do further *in vivo* studies with ^{89}Zr]IIIB6.

Similarly, [^{89}Zr]h-R3-Bz-DFO-NCS was successfully radiolabelled with a purity of 90%. Unbound [^{89}Zr]oxalate was successfully removed by centrifugal separation and a radiochemical purity of 98% was determined for [^{89}Zr]hR3. The radiochemical yield for [^{89}Zr]h-R3, yielding radiochemical [89Zr]h-R3 at 144 MBq with a high tracer concentration of 1570 MBq/ml.

Image guided in vivo characterization of [^{89}Zr]IIIB6

Zr-89 labeling of IIIB6 allowed *in vivo* evaluation of its temporal stability and image-derived biodistribution in athymic nude mice. Upon intravenous tail injection, no adverse events or abnormal behaviour were noted in any of the animals (100%) and micro-PET/CT imaging resulted in superior images, even with injected radioactivity of <8 MBq (i.e. 0.32 MBq/g mouse). Maximum intensity projection (MIP) provided [^{89}Zr]IIIB6 distribution data over 24 h, indicating rapid and high tracer uptake in the liver and spleen as early as 2-4 h post-injection (**Figure 2**). As expected, the presence of the tracer in the cardiovascular system

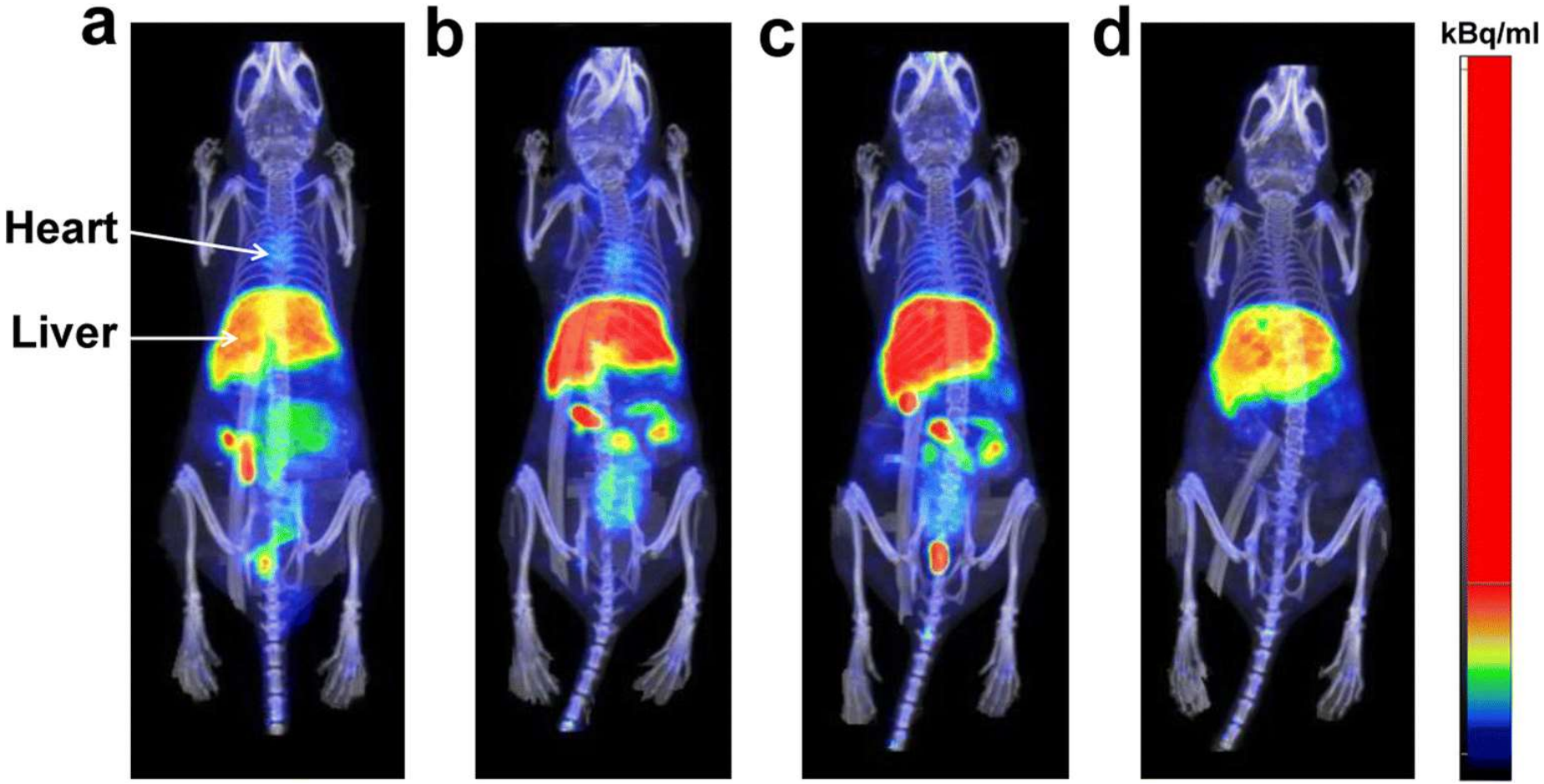

Fig. 2. Representative maximum intensity projections (MIP) of a athymic nude mouse injected with 10.1 MBq [^{89}Zr]IIIB6. Following tracer injection, microPET/CT images were acquisited for 20 min at **a** 2 h, **b** 4 h, **c** 6 h and **d** 24 h. color scale: kilobecquerel per millilitre (blue = minimum, red = maximum).

gradually decreased over time with notable activity remaining at 24 h post-injection. [^{89}Zr]IIIB6-PET/CT showed moderate to minimal uptake in the kidneys followed in order by the lung, stomach, bone and muscle with no uptake in the brain. Some inconsistent activity was observed within the abdominal cavity, which might indicate a possible route of excretion of [^{89}Zr]IIIB6.

The PET/CT image-derived quantification allowed the calculation of the *in vivo* tracer concentrations in the organs/tissue by means of SUVs and volume-of-interest (VOI)-based time-activity curves (**Figure 3**). Analysis of the heart (blood pool) demonstrated an exponential decrease of the tracer over time in an exponential fashion ($y=18.22x^{0.64}$; $R^2=0.978$ (N=10)). The pharmacological half-life was calculated at 9.6 ± 2.5 h ($P<0.006$, unpaired student's t-test, n=3) for [^{89}Zr]IIIB6 which corresponded to 10.9 ± 2.7 g/ml [^{89}Zr]IIIB6.

Maximum SUV values (>10) were determined at 2, 4 and 6 hours in the liver (67 ± 29 g/ml) and spleen (47 ± 10 g/ml) followed by liver followed by the spleen, kidneys, heart, stomach, lung, respectively. Low activity (SUV <10) was present in the bone, whereas muscle tissue (SUV = 0.95-1.67 g/ml) showed the lowest concentration for [^{89}Zr]IIIB6. These low activities are ideal because it does not pose any background signal that would influence the image. The time-activity curves demonstrated a rapid pharmacokinetic behaviour of [^{89}Zr]IIIB6 in organs such as the kidneys and lungs where the maximum tracer concentration was observed as early as 2 h post injection, followed by a significant decrease and the minimum SUV values at 24 h ($P<0.05$). The liver, stomach, bone, and spleen exhibited delayed peak concentrations, similar to the pharmacokinetic behaviour observed for [^{89}Zr]IIIB6 in musculoskeletal tissue, followed by a significant organ washout over time for all these organs except for the spleen ($P=0.246$) and bone ($P=0.298$). The residual radioactivity determined by observing SUV at 24 h post injection (n=3) was 3.7 ± 0.9, 35.4 ± 7.0, 30.5 ± 9.4, 8.7 ± 0.7, 3.2 ± 0.6, 2.2 ± 0.7,

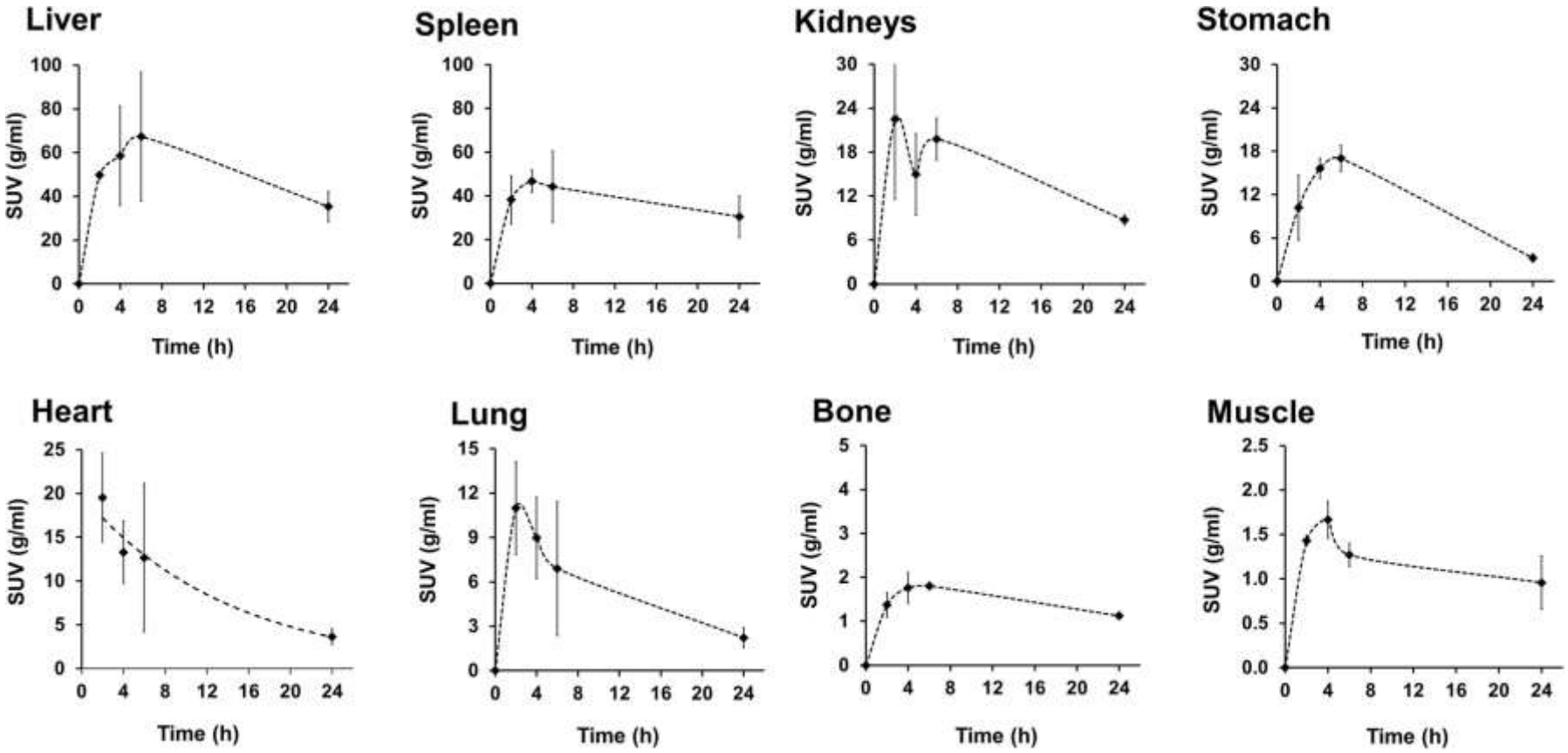

Fig. 3. Time–activity curves derived from VOI analysis of the PET/CT images obtained of the mice injected with [^{89}Zr]IIIB6. Results are displayed as mean (± SEM) for [^{89}Zr]IIIB6 in athymic nude mice ($n = 3$) for organs as indicated.

3.8 ± 1.8 and 1.0 ± 0.3 for the heart, liver, spleen, kidneys, stomach, lungs, bone and muscle tissue, respectively.

Post-mortem biodistribution of [^{89}Zr]IIIB6 and [^{89}Zr]h-R3

The potential of [^{89}Zr]IIIB6 was evaluated by comparing its biodistribution post-mortem with [^{89}Zr]h-R3 and [^{89}Zr]oxalate (negative control) (**Figure 4**). H-R3 is a well studied stable monoclonal antibody approved for human use in tumor imaging and cancer therapy [13]. [^{89}Zr]h-R3was therefore compared to [^{89}Zr]IIIB6 post-mortem to assess the potential of [^{89}Zr]IIIB6 to be used in future as a malaria imaging agent. Maximal uptake of [^{89}Zr]IIIB6 was observed in the kidneys (6.3-9.4 %ID/g), followed by the spleen (5.4 %ID/g) and liver (4.7 %ID/g). All other tissues demonstrated uptake <4.5 %ID/g. [^{89}Zr]IIIB6 shows near-quantitative reduction in whole blood and significant decrease in the vasculature (heart=blood pool; $P<0.01$) over [^{89}Zr]h-R3 24 h post injection; a similar and significantly reduction was also noted in some other organs/tissues (skin, bone and muscle: $P<0.05$). [^{89}Zr]h-R3 displayed an 8-fold higher uptake in blood plasma ($P<0.001$). Due to the fact that [^{89}Zr]oxalate acts similarly to free Zr-89, in the context of having a strong affinity for bone and cartilage [19-21], [^{89}Zr]oxalate is chosen as a negative control to assess the *in vivo* stability of [^{89}Zr]IIIB6 and [^{89}Zr]h-R3. As expected, radioactive accumulation [^{89}Zr]oxalate was greatest in the bone, with an 18-fold higher uptake compared to [^{89}Zr]IIIB6 ($P<0.001$). [^{89}Zr]oxalate demonstrated 2-5 fold higher uptake than [^{89}Zr]IIIB6 in the kidneys and skin ($P<0.05$); and 4-fold lower uptake in the stomach ($P<0.01$). [^{89}Zr]oxalate and [^{89}Zr]IIIB6 uptake into other organs was similar. No significant difference was determined in the uptake of the three tracers in the bladder, spleen, small intestine and liver indicating that these organs are not target organs of the antibodies [^{89}Zr]h-R3 or [^{89}Zr]IIIB6.

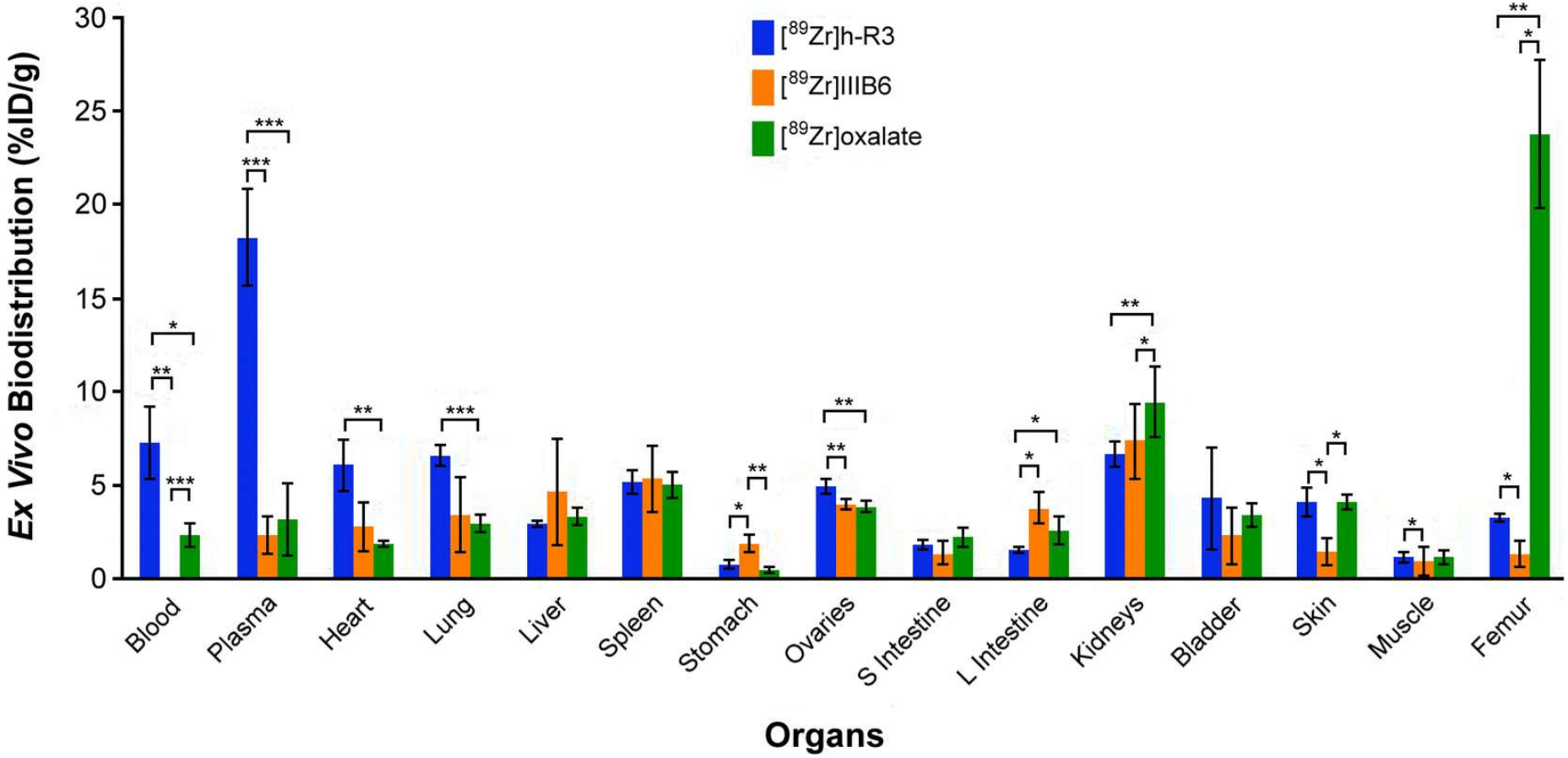

Fig. 4. Comparison of biodistribution showing accumulation of [^{89}Zr]IIIB6 ($n = 5$), [^{89}Zr]h-R3 ($n = 4$) and [^{89}Zr]oxalate ($n = 4$) and in various dissected organs/tissues (24 h post injection) from athymic nude mice. Results are from at least four biological repeats and represented as percentage of injected dose per gram of each organ (%ID/g). *$P < 0.05$; **$P < 0.01$; ***$P < 0.001$.

Discussion

Full length monoclonal antibodies have previously reported to be a suitable vector for radiolabeling and nuclear imaging [22] and here, we for the first time show that these strategies can be applied to antibodies aimed at intracellular malaria parasite. Even though the high molecular weight, immunogenic behaviour and expected long pharmacological half-life pose limitations for the *in vivo* application of IIIB6 [23, 24], PET/CT imaging using an appropriate radioisotope-antibody combination can be of exceptional value as it may enable studying the onset and progression of the disease or may allow for monitoring the effects of drug treatment.

In our study, confocal microscopy imaging allowed for the description of IIIB6 as pan reactive. However, it also revealed the *P. falciparum*-specific nature of IIIB6 including its greater affinity towards the mature asexual and sexual stages. Confocal microscopy imaging was limited to the visualization of IIIB6 binding in *P. falciparum*-ring stages due to the absence of haemozoin crystals in this stage of the IDC [25]. Moreover, the lack of IIIB6 recognition of ring-stage infected erythrocytes suggests that the target antigen of IIIB6 is only expressed on the surface of more mature asexual infected erythrocytes stages (trophozoites and schizonts). Although the actual target for IIIB6 is unknown, these late asexual stages express antigens involved in sequestration on the surface of erythrocytes (e.g. *P. falciparum*-erythrocyte membrane protein 1 (*Pf*EMP1) anchored in Knob-associated histidine rich proteins (KAHRP) which may be a proposed candidate binding partners of IIIB6 [26]. The recognition of trophozoites, schizonts and gametocytes (sequestering parasites) by IIIB6 is of great relevance; in future this antibody may be used to study severe malaria *in vivo* in real time as IIIB6 only recognizes parasite stages that have already entered the IDC. Nevertheless, PET/CT imaging with [^{89}Zr]IIIB6 can be further evaluated as a tool to study these infectious

stages responsible for virulence-associated pathogenicity of malaria, thereby assist in understanding the disease or monitor the disease progression and response to drug treatment.

The employed radiosynthesis was highly efficient, yielding a novel radiolabeled antibody that met the requirements for preclinical application. The accurate formulation of [^{89}Zr]IIIB6 allowed safe intravenous administration into the mice and image-derived *in vivo* evaluation of its biodistribution over time in athymic nude mice. Even with a low injected activity of <8 MBq (i.e. 0.32 MBq/g mouse), the micro-PET/CT imaging obtained resulted in high quality images that allowed successful quantification of the *in vivo* tracer concentrations in the organs/tissue by means of SUVs and volume-of-interest (VOI)-based time-activity curves. Nuclear imaging allowed the characterization of [^{89}Zr]IIIB6 *in vivo*, which had not been explored to date. [^{89}Zr]IIIB6-PET/CT enabled the characterization of the antibody's pharmacokinetic behaviour and stability *in vivo* by way of generating three-dimensional whole body images, representing the antibody influx, organ distribution and excretion in a non-invasive fashion.

Nuclear imaging revealed considerable accumulation of [^{89}Zr]IIIB6 in the blood pool early-on, and persistently-high uptake in liver and spleen over time (despite substantial washout over time). This has no discernible difference between uptake of some other studied Zr-89-labeled anti-cancer antibodies [27] and/or other isotope-labeled antibodies in these two organs [28, 29] possibly due to their nature to remove foreign objects from the blood. Therefore this is an expectable accumulation of radiolabeled antibodies in these two organs. Another factor contributing to this high liver activity is that the route of clearance of an antibody is influenced by the size. Fragments with molecular weights below the renal threshold (~60 kDa) clear through the kidneys while larger fragments i.e. antibodies clear through the hepatobiliary excretion as seen in this study with both h-R3 and IIB6. The

observed clearance of [^{89}Zr]IIIB6 might change once malaria infection is introduced into the host animal, however this was not a particular objective of this study.

The lung VOI observed during PET/CT imaging indicates sufficient diagnostic potential to detect focal uptake of [^{89}Zr]IIIB6.

[^{89}Zr]IIIB6-PET/CT may not be a suitable procedure to study cerebral malaria, as it is evident that IgM antibodies are incapable of crossing the blood brain barrier [30]. Supporting this, it is noted that no brain activity was observed in the PET/CT images.

Image-guided biodistribution provides novel aspects using non-invasive approach to measure the biodistribution of IIIB6 over time. The findings include a low presence in plasma and bone (post-mortem), favourably low background and minor hepatobiliar excretion. The success of isotopic-based imaging is based on the contrast it provides in relation to the target to non-target ratio. Persistent hepatic activity of monoclonal radiolabeled antibodies has been shown to pose a major problem in diagnostics of other diseases [31]. However, in this study we set out just to validate if this antibody's *in vivo* characteristics may meet the requirements to become a future imaging tool to study longitudinal aspects of the complex malaria infections. The great presence of radioactivity in the liver is likely due its high rate of perfusion and some clearance of [^{89}Zr]IIIB6 via the hepatobiliar excretion route. This high uptake and variability of [^{89}Zr]IIIB6 activity (see Fig 3 and 4) in the liver might limit its use in studying/imaging *P. falciparum* infection in the liver of malaria- infected models. However, this can only be determined in an infectious animal model. Similarly, continual splenic activity has been seen in other studies of monoclonal antibodies. This may be due to monoclonal antibodies interacting with specific antigens or being specifically captured by splenic macrophages [32]. Since the lung tissue demonstrated desirable lack of tracer uptake, pulmonary sequestration of malaria parasites could be a suggested imaging scenario facilitated by [^{89}Zr]IIIB6-PET [33].

The impact of a favourable biodistribution will promote further pre-clinical studies [34] but may also indicate eventual organ toxicity of the compound. Therefore, the potential of [^{89}Zr]IIIB6 was evaluated by comparing its biodistribution *post-mortem* with [^{89}Zr]h-R3 and [^{89}Zr]oxalate. As a main finding, the significantly higher uptake of [^{89}Zr]oxalate in the bone compared to that of [^{89}Zr]IIIB6 and [^{89}Zr]h-R3 indicates that these antibody (IIIB6 and h-R3) complexes were stable *in vivo* and did not dissociate significantly from the Zr-89-chelator. This correlates with previous findings that [^{89}Zr]oxalate acts similarly to free Zr-89, in the context of having a strong affinity for bone and cartilage [19-21]. Compared to [^{89}Zr]IIIB6, [^{89}Zr]h-R3 had significantly higher levels of activity presenting in plasma ($P<0.001$) suggesting prolonged [^{89}Zr]h-R3 circulation in the vasculature. This high presence in the plasma suggest that [^{89}Zr]h-R3 has no target organ (the high liver uptake is due to the organ being blood rich) as expected for an EGFR over expressing antibody. Therefore, one expects in a mouse model with an EGFR overexpressing tumour that the labeled antibody will be taken up preferentially. Furthermore, the EGFR receptor background uptake (muscle and skin) was less than anticipated which would allow contrast between an area of increased uptake vs. background. Hence, further studies in xenografted mice (with EGFR tumours) are warranted. [^{89}Zr]IIIB6 did not have a "target" organ other than the expected reticuloendothelial tissue; liver and spleen which suggests that a sufficient part of the injected [^{89}Zr]IIIB6 was excreted. Although certain images indicated that gastrointestinal activity was absent 24 h post injection, assumptions made regarding excretion were limited in that no urine or faeces samples were collected during the experiment.

It remains to be seen what variance occurs for the target to non-target ratio of to determine whether the use [^{89}Zr]IIIB6 in future studies on malaria mice models is acceptable. However, this may require the use of a different radioisotope and/or different targeting agents with

smaller molecular weights (e.g. single-chain variable fragments, aptamers or anti-malarial drugs) and enhanced blood clearance and reduced splenic (scFv) or hepatic involvement. FcFv still contains the Fv (fragment variable) domain preserves antigen binding, but fragments lack the Fc-region allowing eliminating cell-mediated immune interactions. Similarly, aptamers have the same advantage of being non-immunogenic.

Conclusion

This study provides the first proof-of-concept radiolabelling of a *P. falciparum*-specific antibody for *in vitro* and *in vivo* using molecular imaging. Demonstrating the pharmacokinetics of [^{89}Zr]IIIB6 *in vivo* using PET/CT imaging is a much needed prerequisite to further characterise the antibody for prospective studies in malaria-infected animal models. Notable [^{89}Zr]IIIB6 uptake in organs involved in the disease limit the potential of this novel radiotracer.

Acknowledgements

This work was supported by the Nuclear Technologies in Medicine and the Biosciences Initiative (NTeMBI) a national technology platform developed and managed by the South African Nuclear Energy Corporation (Necsa) and funded by the Department of Science and Technology, to JD, TE and JZ. LB received funding from the South African Research Chairs Initiative of the Department of Science and Technology, administered through the South African National Research Foundation (UID84627). Cor Bester (Preclinical Drug Development Platform North West University) is thanked for assisting with the animal handling and Delene van Wyk (Steve Biko Academic Hospital) for assisting with the scintigraphic imaging.

Conflict of interest

The authors declare no conflict of interest.

Compliance with ethical standards

All procedures relating to the [^{89}Zr]IIIB6 study were approved by North West University's AnimCare Ethical Committee (NWU-00042-12-A5). All procedures involving the [^{89}Zr]h-R3 were approved by the Animal Ethics Committee (AEC) of University of Western Australia (RA/3/100/1236).

References

1. Cowman AF, Healer J, Marapana D, Marsh K (2016) Malaria: biology and disease. Cell. 167, 610-624.

2. Mohandas N, An X (2012) Malaria and Human Red Blood Cells. Med Microbiol Immunol. 201, 593-598.

3. Coppens I, Sullivan DJ, Prigge ST (2010) An update on the rapid advances in malaria parasite cell biology. Trends Parasitol. 26, 305-310.

4. Zinn KR, Chaudhuri TR, Szafran AA et al (2008) Noninvasive bioluminescence imaging in small animals. ILAR journal. 49, 103-115.

5. Maude RJ, Barkhof F, Hassan MU et al (2014) Magnetic resonance imaging of the brain in adults with severe falciparum malaria. Mal J. 13, 1.

6. Vaidyanathan S, Patel CN, Scarsbrook AF, Chowdhury FU (2015) FDG PET/CT in infection and inflammation—current and emerging clinical applications. Clin Radiol 70, 787-800.

7. Sathekge M, Maes A, Van de Wiele C (2015). FDG-PET imaging in HIV infection and tuberculosis. Seminars in nuclear medicine; 2013: Elsevier.

8. Sathekge M, Goethals I, Maes A, Van De Wiele, C (2009) Positron emission tomography in patients suffering from HIV-1 infection. Eur J Nucl Med Mol imaging 36, 1176.

9. Kawai S, Ikeda E, Sugiyama M et al (2006) Enhancement of splenic glucose metabolism during acute malarial infection: correlation of findings of FDG-PET imaging with pathological changes in a primate model of severe human malaria. Am J Trop Med Hyg 74, 353-360.

10. Sugiyama M, Ikeda E, Kawai S et al (2004) Cerebral metabolic reduction in severe malaria: fluorodeoxyglucose-positron emission tomography imaging in a primate model of severe human malaria with cerebral involvement. Am J Trop Med Hyg 71, 542-545.

11. Zhang XY, Yang ZL, Lu GM, Yang GF, Zhang LJ (2017) PET/MR Imaging: New Frontier in Alzheimer's Disease and Other Dementias. Front Mol Neurosci 10, 343.

12. Voss SD, Smith SV, DiBartolo N et al (2007) Positron emission tomography (PET) imaging of neuroblastoma and melanoma with 64Cu-SarAr immunoconjugates. Proc Natl Acad Sci 104, 17489-17493.

13. Martínez LMA, Castillo AX, Falcón VNC et al (2014) Development of 90Y-DOTA-nimotuzumab Fab fragment for radioimmunotherapy. Radioanal Nucl Chem 302, 49-56.

14. Christophides GK, Vlachou D, Kafatos FC (2004) Comparative and functional genomics of the innate immune system in the malaria vector Anopheles gambiae. Immunol Rev 198, 127-148.

15. Reader J, Botha M, Theron A et al (2015) Nowhere to hide: interrogating different metabolic parameters of Plasmodium falciparum gametocytes in a transmission blocking drug discovery pipeline towards malaria elimination. Mal J 14, 213.

16. Lambros C, Vanderberg JP (1979) Synchronization of Plasmodium falciparum erythrocytic stages in culture. J Parasitol 418-420.

17. Hoppe H, Verschoor J, Louw A (1991) Plasmodium falciparum: a comparison of synchronisation methods for in vitro cultures. Exp Parasitol 72, 464-467.

18. Holland JP, Divilov V, Bander NH, Smith-Jones PM, Larson S M, Lewis JS (2010) 89Zr-DFO-J591 for immunoPET imaging of prostate-specific membrane antigen (PSMA) expression in vivo. J Nucl Med: official publication, Society of Nuclear Medicine 51, 1293.

19. Deri MA, Zeglis BM, Francesconi LC, Lewis JS (2013) PET imaging with< sup> 89</sup> Zr: From radiochemistry to the clinic. Nucl Med Biol 40, 3-14.

20. Abou DS, Ku T, Smith-Jones PM (2011) In vivo biodistribution and accumulation of ^{89} Zr in mice. Nucl Med Biol 38, 675-681.

21. Abou DS, Ku T, Smith-Jones PM (2011) In vivo biodistribution and accumulation of 89 Zr in mice. Nucl Med Biol 38, 675-681.

22. Van Dongen GA, Visser GW, Lub-de Hooge MN, De Vries EG, Perk LR (2007) Immuno-PET: a navigator in monoclonal antibody development and applications. Oncologist 12, 1379-1389.

23. Hoppin J, Orcutt KD, Hesterman JY, Silva MD, Cheng D, Lackas C, Rusckowski M (2011) Assessing antibody pharmacokinetics in mice with in vivo imaging. J Pharmacol Exp Ther 337, 350-358.

24. Jain M, Venkatraman G, Batra SK (2007) Optimization of radioimmunotherapy of solid tumors: biological impediments and their modulation. Clin cancer res 13, 1374-1382.

25. Delahunt C, Horning MP, Wilson BK, Proctor JL, Hegg MC (2014) Limitations of haemozoin-based diagnosis of Plasmodium falciparum using dark-field microscopy. Malar J 13, 147.

26. Pasternak ND, Dzikowski R (2009) PfEMP1: an antigen that plays a key role in the pathogenicity and immune evasion of the malaria parasite Plasmodium falciparum. Int J Biochem Cell Biol 41, 1463-1466.

27. Jauw YW, Menke-van der Houven CW, van Oordt OHS et al (2016) Immuno-positron emission tomography with zirconium-89-labeled monoclonal antibodies in oncology: what can we learn from initial clinical trials? Front Pharmacol 7.

28. Elsässer-Beile U, Reischl G, Wiehr S et al (2009) PET imaging of prostate cancer xenografts with a highly specific antibody against the prostate-specific membrane antigen. J Nucl Med 50, 606-611.

29. Rolle A-M, Hasenberg M, Thornton CR et al (2016) ImmunoPET/MR imaging allows specific detection of Aspergillus fumigatus lung infection in vivo. Proc Natl Acad of Sci 113, E1026-E1033.

30. Khater N, Kap M, Sayah R, Elbers D, Vriesendorp H (2017) Radiolabeled Immunoglobulin Therapy for Patients with Solid Tumors. J Nucl Med Radiat Ther 8, 2.

31. Boyle CC, Paine AJ, Mather SJ (1992) The mechanism of hepatic uptake of a radiolabelled monoclonal antibody. Int J Cancer 50, 912-917.

32. Cataldi M, Vigliotti C, MoscaT, Cammarota MR, Capone D (2017) Emerging Role of the Spleen in the Pharmacokinetics of Monoclonal Antibodies, Nanoparticles and Exosomes. Int J Mol Sci. 18.

33. Mazhar F, Haider N (2016) Respiratory Manifestation of Malaria: An Update. Int J Med Res Health Sci 5, 59-65.

34. Yip V, Palma E, Tesar DB et al (2014) Quantitative cumulative biodistribution of antibodies in mice: Effect of modulating binding affinity to the neonatal Fc receptor. MAbs 6, 689-696.